

Ligand Binding to Chlorite Dismutase from *Magnetospirillum* sp.

Amy De Schutter,^{†,||} Hugo D. Correia,^{‡,||} Diana M. Freire,^{‡,†} María G. Rivas,[§] Alberto Rizzi,[§] Teresa Santos-Silva,[‡] Pablo J. González,^{*,§} and Sabine Van Doorslaer^{*,†}

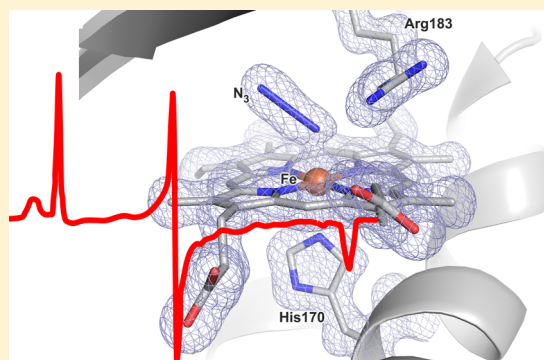
[†]BIMEF Laboratory, Department of Physics, University of Antwerp, Universiteitsplein 1, B-2610 Wilrijk, Belgium

[‡]UCIBIO, REQUIMTE, Departamento de Química, Faculdade de Ciências e Tecnologia, Universidade Nova de Lisboa, 2829-516 Caparica, Portugal

^{*}Departamento de Física, Facultad de Bioquímica y Ciencias Biológicas, Universidad Nacional del Litoral, Ciudad Universitaria, Paraje El Pozo, S3000ZAA Santa Fe, Argentina

Supporting Information

ABSTRACT: Chlorite dismutase (Cld) catalyzes the reduction of chlorite to chloride and dioxygen. Here, the ligand binding to Cld of *Magnetospirillum* sp. (*MaCld*) is investigated with X-ray crystallography and electron paramagnetic resonance (EPR). EPR reveals a large heterogeneity in the structure of wild-type *MaCld*, showing a variety of low- and high-spin ferric heme forms. Addition of an axial ligand, such as azide or imidazole, removes this heterogeneity almost entirely. This is in line with the two high resolution crystal structures of *MaCld* obtained in the presence of azide and thiocyanate that show the coordination of the ligands to the heme iron. The crystal structure of the *MaCld*-azide complex reveals a single well-defined orientation of the azide molecule in the heme pocket. EPR shows, however, a pH-dependent heme structure, probably due to acid–base transitions of the surrounding amino-acid residues stabilizing azide. For the azide and imidazole complex of *MaCld*, the hyperfine and nuclear quadrupole interactions with the close-by ¹⁴N and ¹H nuclei are determined using pulsed EPR. These values are compared to the corresponding data for the low-spin forms observed in the ferric wild-type *MaCld* and to existing EPR data on azide and imidazole complexes of other heme proteins.



INTRODUCTION

Chlorite dismutase (Cld) is a *b*-type heme containing oxidoreductase (EC 1.13.11.49) that catalyzes the reduction of chlorite (ClO_2^-) to chloride (Cl^-) plus dioxygen (O_2).¹ It is essential for (per)chlorate-reducing bacteria (PRB and CRB) because it converts the chlorite anion into innocuous compounds.² ClO_2^- is a strong oxidizing (and potentially cytotoxic) agent transiently produced in the bacterial periplasm during (per)chlorate reduction. Cld is also expressed in nitrite-oxidizing bacteria (NOB) under culture conditions not related to the metabolism of chlorine oxoanions (i.e., chemolithoautotrophic aerobic conditions using nitrite as an electron donor).^{3,4} For that reason, the role of Cld in NOB is not clear and suggests that Cld catalyzes a different reaction from another metabolic pathway occurring in NOB cells.^{3,4} Note that Cld is the only example, besides photosystem II, of an enzyme capable of catalyzing an O–O bond formation.⁵

Anthropogenic activities, such as manufacturing and use of munitions, bleaching agents, and disinfectants, have induced the widespread contamination of drinking and groundwater and soil with chlorine oxoanions (ClO_x^-).⁶ Cld proteins are considered possible candidates in the development of chlorine oxoanion bioremediation processes as well as for biotechnological applications where there is need of a controlled $\text{O}_{2(g)}$

production in oxygen-free environments.¹ All of these potential applications require a good understanding of the substrate specificity, nature of the catalytic redox intermediates, catalytic mechanism, and the different reaction conditions that inactivate Cld.

At present, different Clds from several organisms were isolated either from the original bacteria or from host cells used for heterologous expression (e.g., *E. coli*). All currently known Cld proteins are homomultimeric complexes with each monomer containing one *b*-type heme in the ferric state and an $\alpha\beta$ structure consisting of two similar domains with a ferredoxin fold.¹ There is, however, a large variety in the quaternary structure: Cld from *Nitrobacter winogradskyi*,⁴ *Klebsiella pneumoniae*,⁷ and *Cyanothece* sp. PCC7425⁸ are homodimers; Cld enzymes from *Ideonella dechloratans*⁹ and *Pseudomonas chloritidismutans*¹⁰ are homotetramers (though no X-ray data is available and according to amino acid sequence homology studies they were proposed to be pentamers¹); a

Special Issue: Wolfgang Lubitz Festschrift

Received: April 30, 2015

Revised: August 18, 2015

Table 1. X-ray Crystallography Data Collection Statistics^a

crystal	<i>MaCld_N₃⁻</i>	<i>MaCld_SCN⁻</i>
beamline	PXIII (SLS)	ID23-1 (ESRF)
wavelength (Å)	1.000	0.976
space group	<i>P</i> 2 ₁	<i>P</i> 2 ₁
unit cell		
dimensions (Å)	<i>a</i> = 74.2, <i>b</i> = 133.8, <i>c</i> = 77.6	<i>a</i> = 80.0, <i>b</i> = 124.5, <i>c</i> = 133.4
angles (deg)	β = 113	β = 92.9
Matthews parameter (Å ³ /Da)	2.65	2.62
no. of observed reflections	1 012 788 (43 096)	1 201 104 (60 179)
no. of unique reflections	268 333 (12 762)	261 153 (12 934)
resolution limits (Å)	48.84–1.40 (1.42–1.40)	49.11–1.75 (1.78–1.75)
completeness (%)	98.4 (94.2)	99.7 (99.8)
redundancy	3.8 (3.4)	4.6 (4.7)
CC _{1/2} (%)	99.9 (54.6)	99.8 (71.4)
average <i>I</i> / σ (<i>I</i>)	11.4 (1.4)	12 (2.2)
<i>R</i> _{pim} ^b (%)	3.4 (53.5)	4.6 (35.5)

^aValues in parentheses correspond to data in the outermost shell. ^b $R_{\text{pim}} = \sum_{hkl} [1/(N-1)]^{1/2} \sum_i |I_i(hkl) - \langle I(hkl) \rangle| / \sum_{hkl} \sum_i I_i(hkl)$, where $I_i(hkl)$ is the integrated intensity of a given reflection, $\langle I(hkl) \rangle$ is the mean intensity of multiple corresponding symmetry-related reflections, and N is the multiplicity of a given reflection.

homopentamer structure is found for the Clds of *Dechloromonas aromatica*,¹¹ *Candidatus Nitrospira defluvii*,¹² and *Magnetospirillum* sp.;¹³ and the X-ray crystallographic structure of Cld of *Azospira oryzae* strain GR-1 reveals a homohexameric structure.¹⁴ In spite of the different quaternary structure, in the native (*as-prep*) state of all proteins, the heme group is bound to one imidazole ring of a His, while an Arg residue observed at the distal position of the heme is postulated to play an important role in the stabilization of the substrate and intermediates during enzyme turnover.^{1,5,12}

In a previous work, we have purified a Cld up to electrophoretic grade from cells of the PRB *Magnetospirillum* sp., which were cultured under anaerobic conditions in the presence of perchlorate as a final electron acceptor.¹³ In the present work, we report a combined X-ray crystallography and electron paramagnetic resonance (EPR) study of exogenous ligand binding to the recently identified Cld of *Magnetospirillum* sp., here abbreviated as *MaCld*. The study focuses on the structural effects induced by addition of molecules such as azide, thiocyanate, and imidazole to the *MaCld*.

EXPERIMENTAL METHODS

Protein Purification. *MaCld* was purified up to electrophoretic grade from *Magnetospirillum* sp. cells as described previously.¹³

Total protein was quantified using the bicinchoninic acid kit (Sigma-Aldrich) with bovine serum albumin as a standard, while the concentration of pure *MaCld* was estimated by UV-vis spectroscopy measuring the absorption at 392 nm (Soret band, $\epsilon_{392} = 130 \text{ mM}^{-1} \text{ cm}^{-1}$).¹³

Sample Preparation for EPR Spectroscopy. *MaCld* samples (500 μM) in 50 mM potassium phosphate buffer (KPB, pH 5.5), 50 mM Tris-HCl (pH 7.5), or buffer mix CABS/AMPSO/HEPES/MES/citrate (pH 9.75) were incubated with either 5 mM imidazole (for pH 7.5 and pH 9.75) or sodium azide (pH 5.5 and pH 7.5). Imidazole (≥99%), NaN₃, and sodium azide-1 (terminal-N ¹⁵N-labeled, 98 atm %) were obtained from Sigma-Aldrich. 20% glycerol was added to the samples as a cryoprotectant.

EPR Spectroscopy. X-band continuous-wave (CW) EPR experiments were performed on a Bruker ESP300E spectrom-

eter (microwave (mw) frequency ~9.44 GHz) equipped with a liquid helium cryostat (Oxford Inc.). The EPR spectra were recorded with a modulation amplitude of 0.5 mT and a modulation frequency of 100 kHz. The mw power was 0.63 mW, and the measurement temperature was 7 K.

Pulsed EPR experiments were performed on a Bruker Elexsys E580 spectrometer (mw frequency of 9.76 GHz) equipped with a liquid helium flow cryostat (Oxford Inc.). All experiments were performed at 5 K with a shot repetition rate of 1 kHz.

The two-dimensional ESE (electron spin echo)-detected EPR experiments were performed using the $\pi/2-\tau-\pi-\tau$ -echo sequence, with $t_{\pi/2} = 16$ ns, $t_{\pi} = 32$ ns, and the interpulse distance τ being varied from 88 to 2080 ns in steps of 8 ns.

The HYSCORE (hyperfine sublevel correlation spectroscopy) experiments¹⁵ were performed using the $\pi/2-\tau-\pi/2-t_1-\pi-t_2-\pi/2-\tau$ -echo sequence with pulse lengths $t_{\pi/2} = 16$ ns, $t_{\pi} = 32$ ns, and t_1 and t_2 varied from 96 to 5680 ns in steps of 16 ns. Experiments were performed for different τ values as specified in the figure captions.

Mims ENDOR (electron nuclear double resonance)¹⁶ was performed using the $\pi/2-\tau-\pi/2-T-\pi/2-\tau$ -echo microwave sequence, with a 8.4 μs radiofrequency (rf) π-pulse applied during time T . An ENI A-300 rf amplifier was used. The rf frequency was swept from 1 to 21 MHz in steps of 50 kHz. τ was varied from 96 to 400 ns in steps of 16 ns, and the corresponding spectra were added to remove τ -dependent blind spots.

Davies ENDOR experiments¹⁷ were performed using the $\pi-T-\pi/2-\tau-\pi-\tau$ -echo sequence, with 8 μs rf π-pulse applied during time T . $t_{\pi/2} = 48$ ns, $t_{\pi} = 96$ ns, and $\tau = 220$ ns. The rf frequency was swept from 1 to 21 MHz in steps of 50 kHz. An ENI A-300 rf amplifier was used.

All simulations of the EPR, ENDOR, and HYSCORE spectra were performed with the EasySpin program,¹⁸ a MATLAB toolbox developed for EPR simulations. The HYSCORE data were processed with MATLAB 7.7.0 (The MathWorks, Inc., Natick, MA). The time traces were baseline-corrected with a third-order polynomial, apodized with a Hamming window, and zero-filled. After a two-dimensional Fourier transformation, the absolute spectra were computed. In order to remove blind-spot

effects, the spectra recorded with different τ values were added after Fourier transformation.

Protein Crystallization. Single native crystals of *MaCld* as well as cocrystallized with sodium azide were obtained at 4 °C using the sitting-drop vapor-diffusion method. The crystallizations were performed using an automated crystallization robot (Oryx8, Douglas Instruments), and the precipitating solution contained 16% polyethylene glycol 6000 and 10 mM sodium citrate. The crystallization drops were prepared by adding 1 μ L of the precipitating solution and 1 μ L of ~200 μ M *MaCld* in 50 mM potassium phosphate buffer at pH 6. The cocrystallization assays contained an additional 0.3 mM sodium azide in the precipitating solution. In both cases, crystals appeared after 3 days and grew to their maximum size in 2 weeks. Soaking experiments using the native crystals were performed with 20 mM potassium thiocyanate. After 1 h of soaking, the crystals were transferred to a cryoprotectant solution (16% polyethylene glycol 6000, 10 mM sodium citrate, 20 mM potassium thiocyanate, and 25% glycerol) for a few seconds and were then flash-frozen with liquid nitrogen. *MaCld* samples cocrystallized with sodium azide were also flash-frozen using the same cryoprotectant containing 0.3 mM sodium azide instead of potassium thiocyanate.

Data Collection, Processing, and Refinement. Complete data sets were collected at the PXIII beamline (Swiss Light Source, Villigen, Switzerland) and at the ID23-1 beamline (European Synchrotron Radiation Facility, Grenoble, France) for the structures with azide and thiocyanate, respectively. For the *MaCld_N₃*⁻ crystals, a complete data set was collected at 1.00 Å wavelength up to 1.40 Å maximum resolution, while, for the *MaCld_SCN*⁻ crystals, data were collected at 0.976 Å wavelength and the crystals diffracted up to 1.75 Å resolution. The data were processed using XDS¹⁹ and scaled using Aimless²⁰ from the CCP4 suite.²¹ Data collection statistics are presented in Table 1.

The phase problem was solved by molecular replacement using Phaser²² with the model of the homologue Cld from *Dechloromonas aromatica* (PDB accession code: 3Q08). The structures were refined using restrained refinement in Refmac5²³ and manual model building in Coot.²⁴ PDB_REDO²⁵ was used to perform constructive validation and structure rerefinement. Anisotropic refinement was performed in the case of the 1.40 Å resolution *MaCld_N₃*⁻ structure. Geometrical validation was carried out by Procheck²⁶ and Molprobity.²⁷ Refinement statistics are presented in Table 1.

RESULTS AND DISCUSSION

Structural Characterization. Cld from *Magnetospirillum* sp. crystallizes in the *P*2₁ space group as previously reported.¹³ In the present work, we have crystallized *MaCld* in the presence of azide and thiocyanate and the crystals diffracted to high resolution. These crystals also belong to the same space group, but the cell dimensions and the crystal packing are quite different in the two cases (Table 1): while the asymmetric unit of the *MaCld_N₃*⁻ crystals contains one homopentamer, the asymmetric unit of *MaCld_SCN*⁻ contains two homopentamers. Considering the overall structure of each homopentamer, the five ~28 kDa subunits are arranged in a “donut-like” shape with a height of ca. 65 Å and inner and outer diameters of ca. 20 and 73 Å, respectively (Figure 1A).

The two X-ray structures here reported (*MaCld_N₃*⁻ and *MaCld_SCN*⁻) are structurally very similar to an rmsd of 0.14–0.45 Å upon superposition of all the C α atoms from the

Table 2. Crystal Structure Refinement Statistics

data set	<i>MaCld_N₃</i> ⁻	<i>MaCld_SCN</i> ⁻
PDB code	SA12	SA13
resolution limits (Å)	48.84–1.40	49.11–1.75
wavelength (Å)	1.000	0.976
R-factor (%)	11.79	15.13
no. of reflections	254 758	248 487
R-free (%)	15.43	18.35
no. of reflections (R-free)	13 525	12 628
no. of residues	1210	2426
no. of atoms	11 683	21 916
rmsd bond length (Å)	0.011	0.017
rmsd bond angles (deg)	1.517	1.781
average temperature factor (Å ²)		
main chain atoms	17.2	16.6
side chain atoms	20.6	20.2
water molecules	33.9	26.0
Ramachandran plot (%)		
residues in most favored regions	93.5	93.4
residues in additionally allowed regions	6.5	6.6
residues in generously allowed regions	0.0	0.0
residues in disallowed regions	0.0	0.0
overall G-factor	0.09	0.01

different monomers. Structural superposition of the monomers within the *MaCld_N₃*⁻ or *MaCld_SCN*⁻ homopentamer yielded rmsd values between 0.14 and 0.39 Å for all C α atoms. Furthermore, structural alignments of a Cld monomer from *Magnetospirillum* sp. with those of other homopentameric Cls (*Dechloromonas aromatica* (3Q08) and *Candidatus Nitrospira defluvii* (3NN1)) showed a high degree of structural similarity with rmsd values ranging between 0.60 and 1.10 Å.

Each Cld monomer presents a $\alpha\beta$ structure, consisting of two ferredoxin-like fold domains (Figure 1B). As observed in Cls from other organisms, there are eight-stranded antiparallel β -sheets present in the structure. Each of the two ferredoxin-like fold domains presents a four-stranded antiparallel β -sheet forming β -barrels composed by 4 \uparrow 1 \downarrow 3 \uparrow 2 \downarrow and 8 \uparrow 5 \downarrow 7 \uparrow 6 \downarrow , which are flanked on both sides by α -helices on the external face of the protein monomer. The heme-*b* cofactor is located in a hydrophobic cavity comprised between the β -barrels 8 \uparrow 5 \downarrow 7 \uparrow 6 \downarrow and the flanking α -helices (Figure 1B). In both *MaCld_N₃*⁻ and *MaCld_SCN*⁻ structures, the heme *b* is surrounded by several amino-acid residues which interact and stabilize the cofactor through hydrophobic (alkyl–alkyl, π –alkyl, π – π stacking), H-bonding (classical and π -donor H-bonding observed for Thr₁₇₁ and Thr₁₇₄), and electrostatic interactions (Figure 2A–C).

In both X-ray structures, the Fe³⁺ atom is hexacoordinated to six N atoms: four from the porphyrin, one from the exogenous ligand (azide or thiocyanate), and the last one from the imidazole side chain of His₁₇₀ (Figures 2A,B and 3). An important feature in the heme environment already observed in other Cld structures with confirmed chlorite dismutase activity is the hydrogen bond that exists between the His₁₇₀ and Glu₂₂₀ at a distance of ca. 2.7 Å (Figure 2B). Similarly to the triad Asp-His-Fe³⁺ observed in peroxidases,²⁸ the interaction between Glu₂₂₀-His₁₇₀-Fe³⁺ (Figure 2B) might be important to maintain a high-spin pentacoordinated iron in the absence of the substrate or an exogenous ligand, defining the redox properties (turning the reduction potential of the Fe³⁺/Fe²⁺ couple more

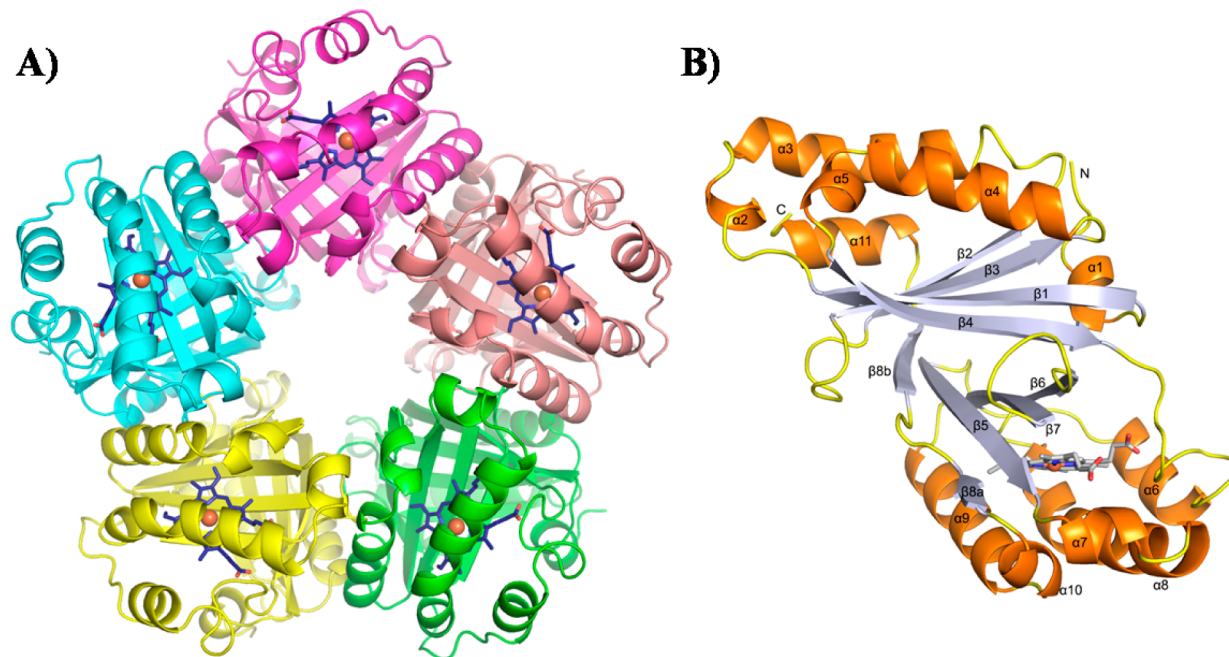


Figure 1. Crystallographic structure of Cld from *Magnetospirillum* sp. (A) The homopentameric quaternary structure is shown colored by polypeptide chain, hemes in blue, and the iron atom as an orange sphere. (B) Secondary structure: the α -helices (orange) and β -strands (cyan) are labeled according to the ferredoxin fold. The heme cofactor is shown in atom color code (carbon, gray; nitrogen, blue; oxygen, red).

negative) and allowing the stabilization of higher oxidation states of the iron heme (i.e., $\text{Fe}^{\text{IV}}=\text{O}$), which are proposed catalytic intermediates during chlorite reduction.

In both *MaCld*_{N₃}⁻ and *MaCld*_{SCN}⁻ crystals, the ligands are directly bound to the heme Fe^{3+} ion and are stabilized by H-bonds to the guanidinium group from the side chain of Arg₁₈₃. Both ligands are found between Arg₁₈₃ and the hydrophobic pocket created by the side chains of Leu₁₈₅, Thr₁₉₈, and Phe₂₀₀. Clear electron density can be observed for the heme cofactor, the Fe atom, and both ligands, azide and thiocyanate, due to the high resolution of the data and the high occupancy of the ligands (Figure 3). Both ligands were refined with full occupancy in all monomers present in the asymmetric units of both crystals with B-factors similar to the heme and neighboring residues. The azide molecule in the *MaCld*_{N₃}⁻ structure is coordinated to the Fe atom of the heme cofactor by one N atom at distances between 1.92 and 2.05 Å among the five monomers. Similarly, the thiocyanate ion was also found coordinating the heme iron by the N atom at distances between 1.92 and 2.16 Å among the 10 monomers in the *MaCld*_{SCN}⁻ structure. Clear electron density for the heavier S atom was observed in the opposite end to the Fe, indicating that this is the binding mode of the thiocyanate anion (isothiocyanate: $\text{N}=\text{C}=\text{S}$).

EPR Analysis. In our recent work,¹³ we showed that the heme site of ferric wild-type *MaCld* in frozen solution is strongly influenced by the type of the buffer and the presence/absence of salt ions. Under some conditions, a large variety of high-spin (HS, $S = 5/2$) and low-spin (LS, $S = 1/2$) states of the ferric heme iron were found to coexist.¹³ This was also observed for Cld from *Azospira oryzae* strain GR-1,¹⁴ *Nitrobacter winogradskyi*,²⁹ *Candidatus "Nitrospira defluvii"*,²⁹ *Klebsiella pneumoniae*,⁷ and *Dechloromonas aromatic*⁷ and for the recombinant Cld from *Ideonella dechloratans*.³⁰ Moreover, a similar heterogeneity depending on pH and buffer types was also found for *Mycobacterium tuberculosis* catalase-peroxidase

(KatG).³¹ The different heme forms of KatG are even interconverting over storage time,³¹ an effect also observed by us for *MaCld* (Supporting Information, Figure S1).

Particularly intriguing is the formation of LS ferric heme states, since they imply the distal binding of strong exogenous or endogenous bases to the heme iron. Figure 4 shows the LS heme contributions to the EPR spectrum of ferric wild-type *MaCld* at pH 9.75 after 20 days of storage in the freezer and a number of freeze-thaw cycles (full spectrum, including high-spin components, is shown in the Supporting Information, Figure S1). No less than five LS ferric heme complexes contribute to the spectrum (Figure 4, Table 3). Complexes LS3–5 have principal g values typical of hydroxide adduct ferric heme proteins.^{7,9,32} This assignment is supported by the lack of these species at lower pH values (Supporting Information, Figure S2). The observation of several hydroxide adduct contributions with slightly different EPR parameters indicates a variation of open and/or closed conformers in which the hydroxide ligand can assume different orientations. Interestingly, two sets of hydroxide adducts with g -values (2.56, 2.18, 1.87) and (2.64, 2.18, 1.82) were also detected for Cld of *D. aromatic* at pH 8.0,⁷ and were related to the existence of a closed and open conformer of the protein, believed to be linked to a conformational adjustment of Arg₁₈₃.³³ Possibly, a similar rearrangement of the Arg₁₈₃ is responsible for the three observed hydroxide adducts of *MaCld*.

The nature of LS1 and LS2 is less obvious. They are present at pH 5.5, 7.5, and 9.75 (Figure 4, Figure S2). LS2-like signals have been observed for other Cls (Table 3) and have been associated with possible distal ligation of imidazoles or histidine.^{14,30} In order to determine which of the LS forms are still susceptible to binding of endogenous ligands, we studied the effect of addition of ligands, such as azide and imidazole, on the EPR spectra of ferric *MaCld*.

Addition of azide to a solution of *MaCld* almost fully lifts the heterogeneity of the EPR spectrum (Figure S3, Figure 5). In

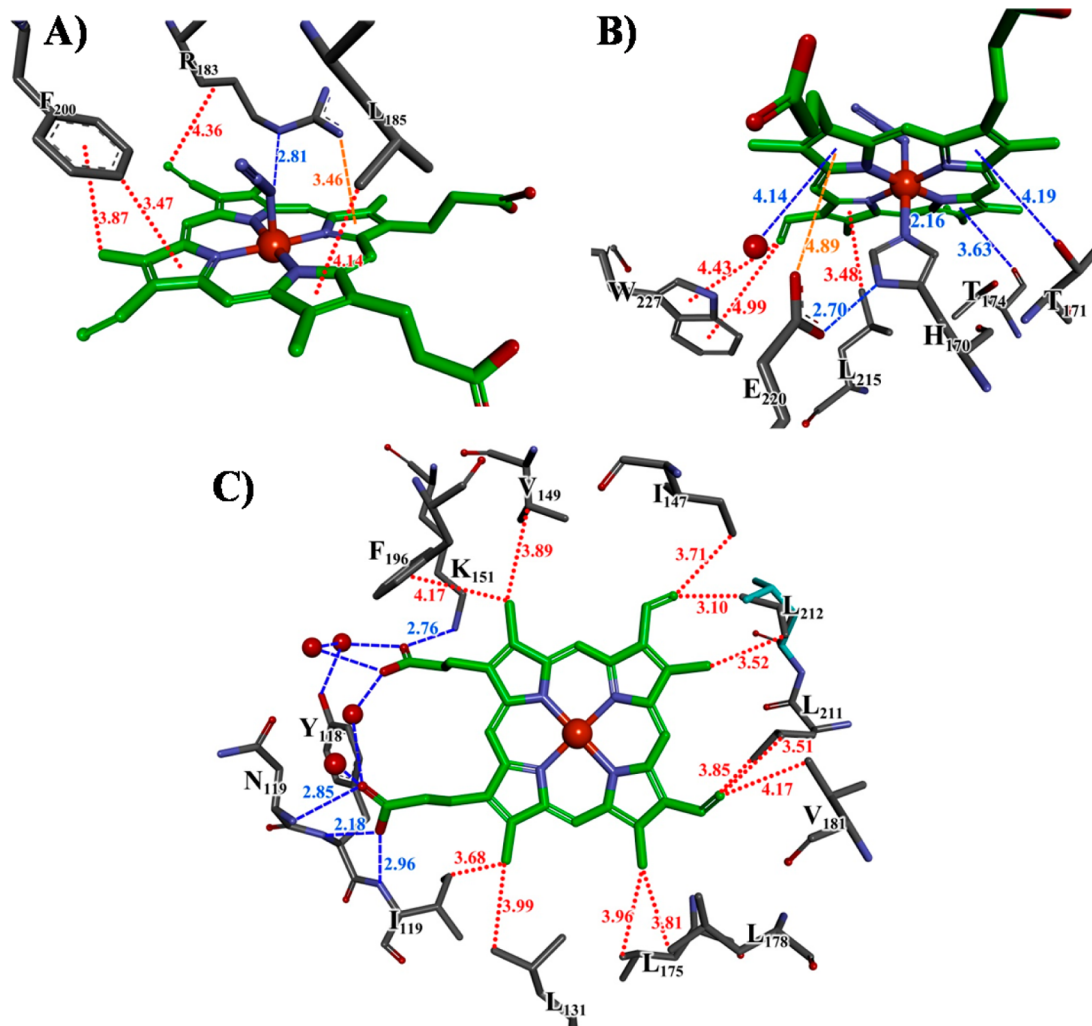


Figure 2. $\text{MaCld}_\text{-N}_3^-$ structure showing heme-*b* stabilization by nonbonding interactions with surrounding amino acids located at the distal (A) and proximal (B) sides. The top (from distal side) view (C) shows amino-acid residues and water molecules interacting with the propionates, methyl, and ethylene groups of the porphyrin ring. Atom color code: gray, carbon; green, heme carbon atoms; blue, nitrogen; red, oxygen. Orange and red spheres are the iron atom and water molecules, respectively. Interactions are shown as dashed lines, and distances are in Å: blue, H-bond; red, hydrophobic alkyl–alkyl, π -alkyl, and π - π stacking; orange, electrostatic. (3D structures and nonbonding interactions were drawn with Accelrys Discovery Studio Visualizer v.4.1.)

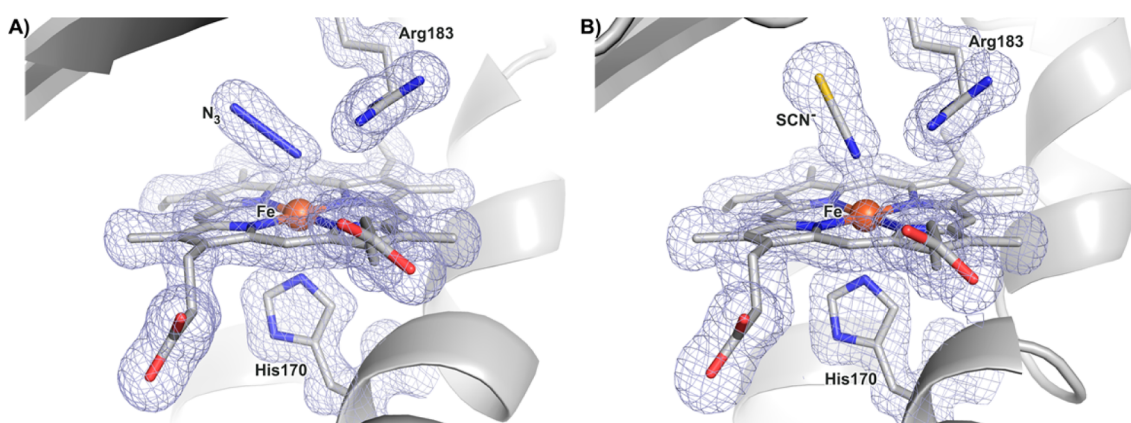


Figure 3. Crystallographic structures of (A) $\text{MaCld}_\text{-N}_3^-$ and (B) $\text{MaCld}_\text{-SCN}^-$. Representation of the active site coordination: both azide and thiocyanate were modeled with an occupancy factor of 1. Atom color code: C in gray, N in blue, O in red, S in yellow, and Fe in orange. The blue mesh represents the 2mFo–DFc maps, which are contoured at 1σ .

our previous work,¹³ we observed that Cld batches showing high heterogeneity in the EPR spectrum (purified using a

combination of Tris–HCl and MES buffers) yielded kinetic parameters identical to Cld batches showing only a Fe^{3+} –heme

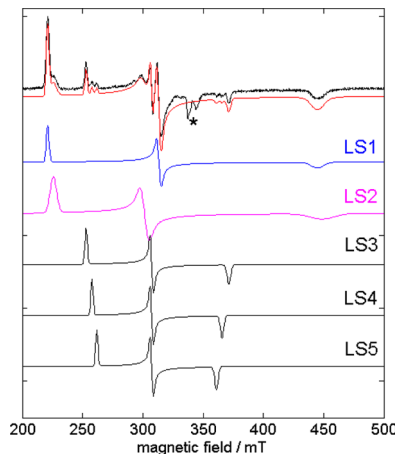


Figure 4. Experimental (black) and simulated (red) X-band CW-EPR spectra of a frozen solution of ferric wild-type *MaCld* at pH 9.75. The individual EPR contributions LS1–5 used to simulate the spectra are also shown. The corresponding principal *g* values are given in Table 3. * indicates the high-field signals of the high-spin contributions (see also the Supporting Information, Figure S1).

high spin species (purified using exclusively phosphate buffer). This indicates that the heterogeneity may also be removed by the substrate (chlorite) and that the different HS and LS species are not dead/inactive Cld forms.

At pH 7.5, all but one of the EPR contributions (LS2) found for the native *MaCld* disappear with a concomitant appearance of a new EPR signal that is typical of an LS heme iron (Figure 5a, component LSAz1). The principal *g* values of LSAz1 are similar to those observed for azide-ligated myoglobin³⁵ (Table 4). The experiment thus reveals that the vast majority of all different HS and LS ferric heme forms observed with EPR in the native protein are in a “ready” state, i.e., accessible to external ligands, and can be converted to the same state (see also further discussion in the Supporting Information). Addition of sodium azide to *MaCld* at pH 5.5 shows the presence of two LS heme forms (LSAz1 and LSAz2) with slightly different principal *g* values (Figure 5b, Figure S4). LSAz1 is still dominant at this lower pH value ($84 \pm 3\%$). Two

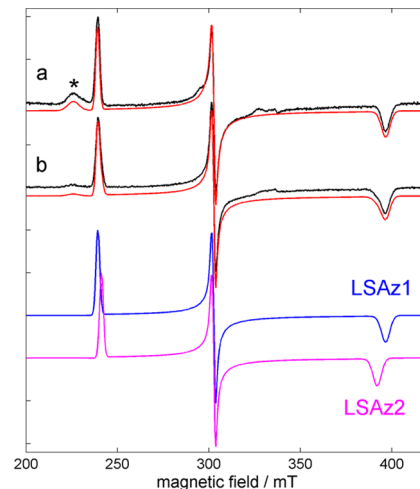


Figure 5. Experimental (black) and simulated (red) X-band CW-EPR spectra of a frozen solution of azide-bound *MaCld* at pH 7.5 (a) and pH 5.5 (b). The individual EPR contributions LSAz1 and LSAz2 used to simulate the spectra are also shown. * indicates a contribution of a nonactive form of the protein already present in the native *MaCld* sample (LS2, Figure 4 and Figure S3).

LS ferric heme forms were also found for the azide complex of the His₆₄ → Thr mutant of horse heart myoglobin (hhMb).³⁶ In contrast to azide-ligated wild-type hhMb in which the azide ligand is stabilized by the distal histidine (His₆₄), no distal amino acid is stabilizing azide in the His₆₄ → Thr variant. Depending on the water occupancy of the distal heme pocket, the azide molecule then can assume two orientations. In the *MaCld*_N₃⁻ crystallographic data (Figures 2 and 3), the azide ligand is stabilized by the guanidinium group of the Arg₁₈₃ side chain and occupies one defined position, in agreement with the dominant LS species (LSAz1) observed for *MaCld* samples incubated with sodium azide at pH 7.5. Therefore, the observed pH-dependent heterogeneity may be due to direct acid–base chemistry at the Arg₁₈₃ or to remote interactions with amino acids undergoing acid–base transitions that interact with the active site cavity modifying the azide orientation in the heme pocket. Similar pH-dependent effects were observed exper-

Table 3. Principal *g* Values of the LS Ferric Heme Contributions in the EPR Spectrum of Wild-Type *MaCld* at pH 9.75 for the Specific Conditions of Protein Purification and Storage Mentioned in the Text^a

		<i>g_x</i> (±0.001)	<i>g_y</i> (±0.001)	<i>g_z</i> (±0.001)	relative contribution (±1%)	reference
<i>MaCld</i> (pH 9.75)	LS1	1.515	2.151	3.049	60	this work
	LS2	1.500	2.235	2.985	24	
	LS3	1.815	2.193	2.665	11	
	LS4	1.843	2.193	2.615	3	
	LS5	1.867	2.193	2.575	2	
<i>NdCld</i>		~1.2	2.13	3.14	n.r.	29
		1.47	2.25	2.99	n.r.	
<i>NwCld</i>		~1.2	2.12	3.15	100	29
<i>AoCld</i>		1.49	2.23	2.97	n.r.	14
		1.55	2.26	2.90	n.r.	
<i>IdCld</i> (pH 8.9)		1.87	2.19	2.56	100	9
<i>KpCld</i> (pH ≥ 8.0)		n.r.	n.r.	3.10	n.r.	7
		1.87	2.19	2.54	n.r.	
rec <i>IdCld</i> (pH 7)		1.52	2.25	3.04	100	30

^aA comparison with LS components observed in other systems is given. (NdCld = Cld from *Candidatus Nitrospira defluvii*, NwCld = Cld from *Nitrobacter winogradskyi*, AoCld = Cld from *Azospira oryzae* strain GR-1, IdCld = Cld from *Ideonella dechloratans*, rec IdCld = recombinant IdCld, KpCld = Cld from *Klebsiella pneumoniae*, n.r. = not reported).

Table 4. Principal *g* Values of Azide-Ligated and Imidazole-Ligated *MaCld* in Comparison with Those Reported for Azide and Imidazole Complexes of Related Heme Proteins^a

sample		<i>g_x</i>	<i>g_y</i>	<i>g_z</i>	reference
Azide-Ligated Heme Proteins					
<i>MaCld</i> + NaN ₃ (pH 7.5)	LSAz1	1.70 ± 0.01	2.228 ± 0.005	2.820 ± 0.005	this work
<i>MaCld</i> + NaN ₃ (pH 5.5)	LSAz1	1.700 ± 0.005	2.228 ± 0.005	2.820 ± 0.005	this work
	LSAz2	1.720 ± 0.005	2.228 ± 0.005	2.795 ± 0.005	
HN ₃ + catalase		1.74	2.18	2.80	34
swMbN ₃		1.72	2.22	2.80	35
hhMbN ₃		1.72	2.21	2.80	36
hhMb(His64Thr)N ₃		1.69	2.18	2.88	36
		1.73	2.18	2.88	
CarpHbN ₃ (pH 4)		1.61	2.18	2.87	38
CarpHbN ₃ (pH 8)		1.67	2.19	2.81	38
Imidazole-Ligated Heme Proteins					
<i>MaCld</i> + Im (pH 7.5 + pH 9.75)	LSIm	1.48 ± 0.01	2.25 ± 0.01	2.99 ± 0.01	this work
GR-1 CldIm (pH 7)		1.51	2.25	2.96	32
hhMbIm		1.49	2.25	2.953	39

^aswMb = sperm whale myoglobin, hhMb = horse heart myoglobin, hhMb(His64Thr): His64 → Thr mutant of horse heart myoglobin.

Table 5. Principal ¹⁴N Hyperfine (*A*) and Quadrupole (*Q*) Values of Imidazole-Ligated *MaCld* (LSIm) and LS1 (This Work) in Comparison with Those of hhMbIm^{39,a}

	<i>A_x</i> (MHz)	<i>A_y</i> (MHz)	<i>A_z</i> (MHz)	<i>Q_x</i> (MHz)	<i>Q_y</i> (MHz)	<i>Q_z</i> (MHz)	<i>α, β, γ</i> (deg)
<i>MaCld</i> - LSIm							
heme 1	-4.7 (±0.2)	-4.7 (±0.2)	-5.7 (±0.1)	-0.52 (±0.05)	0.85 (±0.10)	-0.33 (±0.05)	10, 0, 0 (±10)
heme 2	-5.3 (±0.2)	-5.4 (±0.2)	-6.4 (±0.1)	-0.52 (±0.05)	0.85 (±0.10)	-0.33 (±0.05)	110, 0, 0 (±10)
His or Im	-6.0/-5.6 (±0.2)	-5.2/-4.9 (±0.2)	-5.1/-5.1 (±0.1)	0.32 (±0.05)	0.38 (±0.05)	-0.90 (±0.10)	40, 0, 0 (±20)
hhMbIm							
heme 1	n.d.	n.d.	-5.6 (±0.1)	-0.40 (±0.1)	0.90 (±0.2)	-0.50 (±0.1)	n.d.
heme 2	n.d.	n.d.	-6.2 (±0.1)	-0.40 (±0.1)	0.90 (±0.2)	-0.50 (±0.1)	n.d.
His/Im	n.d.	n.d.	-5.0 (±0.1)	n.d.	n.d.	-0.85 (±0.10)	n.d.
<i>MaCld</i> - LS1							
heme 1	n.d.	n.d.	-6.0 (±0.1)	n.d.	n.d.	-0.36 (±0.05)	n.d.
heme 2	n.d.	n.d.	-6.4 (±0.1)	n.d.	n.d.	-0.36 (±0.05)	n.d.
His	n.d.	n.d.	-5.7 (±0.1)	n.d.	n.d.	-0.80 (±0.10)	n.d.

^aThe Euler angles α , β , and γ in the *g*-tensor frame are given. n.d. = not determined.

imentally for wild-type Cld from *D. aromatica*³³ and suggested for Cld from *Candidatus Nitrospira defluvii* on the basis of molecular dynamics computations.³⁷ Interestingly, a pH dependence was also observed for the azide complex of carp (*Cyprinus carpio*) methemoglobin.³⁸ However, in contrast to the current case, an increase of the *g* anisotropy was observed upon lowering of the pH. The changes were interpreted in terms of an increase of the out-of-plane displacement of the iron atom and stabilization of the T-form of the carp azidomethemoglobin at high proton concentration. The T-form is specific for the hemoglobin case and may explain the different pH-dependent behavior.

Addition of imidazole to wild-type *MaCld* also leads to a disappearance of the heme-form heterogeneity (Supporting Information, Figure S5). A single low-spin ferric heme form (LSIm) with parameters close to those earlier reported for other imidazole complexes of Cld is formed (Table 4). The principal *g* values of LSIm are also similar to those found for the LS2 state, supporting the earlier suggestions that imidazole or His ligation could cause the latter signal.^{14,30} Histidine ligation can, however, be ruled out for *MaCld* LS2 on the basis that no His is present on the distal side of the heme pocket. Furthermore, no imidazole was added during the purification process. Possibly, binding of another buffer molecule may lead

to LS2 formation, but this cannot be confirmed at this stage. In any case, azide binding to the heme ligand is blocked in the LS2 state. Azide generally binds well to heme proteins. However, Dubois and co-workers found that, in *D. aromatica* Cld, the binding affinity of azide is comparable to that of imidazole and lower than that of KCN, and that in certain Cld variants azide does not bind to the heme while imidazole and cyanide do. Therefore, it is not surprising that azide is not able to replace all distal ligands.

The principal *g* values of LSIm agree with a dihedral angle between the imidazole planes of the proximal His₁₇₀ and distal Im ligand in the order of 20–30°.^{40,41} *MaCld* crystals soaked with imidazole (*MaCld*_Im) diffracted up to ~3.0 Å using synchrotron radiation. Owing to the low resolution of our data, the refinement could not be finished and for this reason our *MaCld*_Im structure was not deposited. Nevertheless, we could observe electron density indicating that the exogenous imidazole ligand occupied the axial position at the distal side. The only existing X-ray crystallography structure of a Cld-imidazole complex was reported for *Candidatus Nitrospira defluvii* (NdCld).¹² In this 1.85 Å resolution structure, the exogenous imidazole occupies the same position with nearly the same orientation that we observed in our low-resolution data, showing a dihedral angle of 25° between His and the Im plane

(Supporting Information, Figure S6). This structural similarity is further confirmed by the ^{14}N HYSCORE analysis of LSIm (see Table 5, Figure 6, Supporting Information (Figures S7–

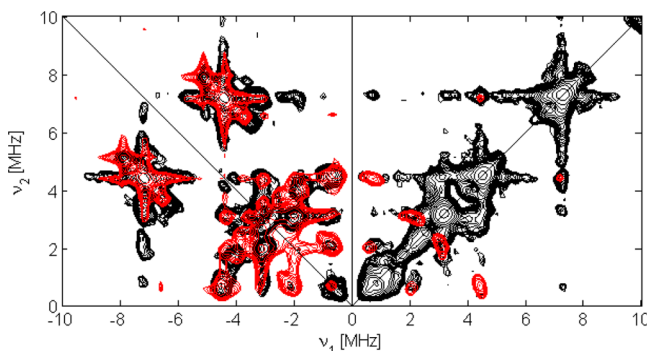


Figure 6. Experimental (black) and simulated (red) X-band ^{14}N HYSCORE spectrum of a frozen solution of the imidazole complex of ferric MaCld (LSIm) recorded at an observer position corresponding with $g = g_z$. The spectra are the sum of the HYSCORE spectra for interpulse distance $\tau = 88, 96, 176$, and 200 ns. The simulation includes the contributions of the heme, His, and Im ^{14}N nuclei (Table S5).

S9) for detailed analysis following the general procedure outlined in ref 42). This analysis reveals similar Euler angles for the ^{14}N hyperfine tensors of the iron-binding ^{14}N of both axial ligands (His_{170} and Im), which indicates nearly parallel orientation of the two imidazole planes (Table 5). The data agree with an average angle of 30° between the $\text{N}_{\text{heme}}-\text{Fe}-\text{N}_{\text{heme}}$ axis and the projection of the imidazole planes on the heme plane (Figure S10, Supporting Information). Furthermore, in line with earlier observations for imidazole complexes of myoglobins,^{39,43} the heme nitrogens are found to be two-by-two magnetically inequivalent (Table 5).

It is interesting at this point to compare the pulsed EPR data of LSIm with those of the unknown LS1 state and of MaCldN_3^- (LSAz1). There is a striking difference in the ^1H HYSCORE spectra taken at $g = g_z$ for LS1 and LSIm (Figure 7). The ^1H HYSCORE spectrum of LSIm is typical of many bis-imidazole coordinated heme proteins, showing (1) the broad ridge of the proximal His_{170} protons closest to the heme iron (~ 3.2 MHz in width) and (2) a second (narrower) ridge stemming from the more remote protons (Figure 7a). In contrast, the ^1H HYSCORE spectrum of LS1 reveals, besides

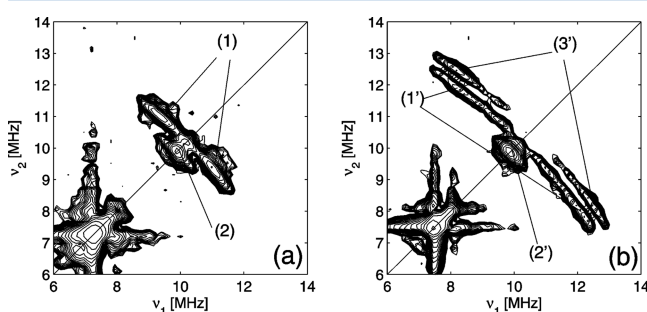


Figure 7. Experimental ^1H HYSCORE spectra of a frozen solution of (a) LSIm and (b) LS1. The spectra were in both cases recorded at $g = g_z$, and are the sum of the HYSCORE spectra for interpulse distance $\tau = 88, 96, 176$, and 200 ns. The cross peak centered at ~ 7.5 MHz stems from ^{14}N hyperfine/quadrupole interactions.

the ridge of the remote protons (labeled (2')), two ridges that are displaced differently along the diagonal (Figure 7b (1') and (3'))), with a total width of 5 MHz. In Figure S11, an overlay of the two spectra is shown. The two proton ridges in the LS1 case extend much further along the antidiagonal. These cannot be ascribed to the proximal His_{170} protons. The ridge of the latter protons is partially buried by the ridge (1') (Figure S11). This is also confirmed in the ^1H ENDOR analysis (Figure S12). Furthermore, the maximum ^1H hyperfine coupling (~ 4 MHz) observed for LSAz1 at $g = g_z$ lies in between the values obtained for LS1 and LSIm (Figure S12), with only two ^1H HYSCORE ridges (one broader, one narrower) visible at this observer position (Figure S13). For LSAz1, the displacement Δ along the diagonal of the broadest ridge versus (ν_H, ν_H) (ν_H = proton Larmor frequency) is the same as that found for ridge (1) of LSIm (Figure 7a), namely, 0.027 ± 0.03 MHz. The displacement of such a ^1H HYSCORE ridge is directly related to the dipolar part of the hyperfine interaction.⁴⁴ The same value of Δ thus indicates that the features stem from protons at the same distance from the iron center in both heme pockets. As follows from the crystal structure of MaCld-N_3^- , these can only be the protons of the proximal His_{170} that are closest to the iron center (Figure 3A). The small difference in the maximum ^1H hyperfine coupling (3.15 versus 4 MHz) observed for LSIm and LSAz1 can be ascribed to a small difference in the Fermi contact term, which is directly related to the difference in the electronic structure. The significantly larger displacement Δ of ridge (3') (0.58 ± 0.03 MHz) and the overall large maximum extent of the ridge indicate that there is a proton present in LS1 that is significantly closer to the iron center than that found for the imidazole and azide complexes of MaCld. This proton cannot stem from coordination of water to the heme iron, since water is a weak ligand which will lead to a HS form.

Furthermore, the hyperfine parameters of the heme and His_{170} nitrogens differ between LS1, LSIm, and LSAz1. Although a full analysis of these interaction parameters for LS1 is not possible due to the overlap of the EPR spectra of the different low-spin forms (LS1–LS5, Figure 4), we can obtain the z -components of the hyperfine and nuclear quadrupole tensor from analysis of the ^{14}N HYSCORE spectrum measured at a magnetic field position agreeing with $g = 3.049$ (g_z of LS1) (Figure 8, Table 5). We notice a significant increase in the hyperfine value of the His_{170} side-chain nitrogen atoms of LS1 in comparison to the LSIm case, suggesting a different Fe–N distance and/or rotation of the imidazole plane of the proximal His_{170} . Together with the large change in the ^1H hyperfine interactions (Figure 7), this indicates a considerable distortion of the heme region in LS1, possibly caused by a large (buffer) molecule acting as an external ligand. In the crystal structure of Cld from *Dechloromonas aromatic*a, a buffer 2-(*N*-morpholino)-ethanesulfonate (MES) molecule is found hydrogen bonded to the distal Arg₁₈₃, showing that buffer molecules may approach the heme region in chlorite dismutase.¹¹ In fact, Arg₁₈₃ has been suggested to gate substrate entry.¹¹

^{14}N HYSCORE also allows the determination of the hyperfine and nuclear quadrupole interactions of the iron-bound heme and His_{170} nitrogens in LSAz1 (Table 6, Supporting Information, Figures S14–S16). The most marked differences with LSIm and LS1 (Table 5) are found for the His hyperfine and quadrupole values. This is not unexpected, since the binding of His_{170} to the heme iron will be affected by the sixth ligand, which is in LSIm a neutral imidazole molecule and

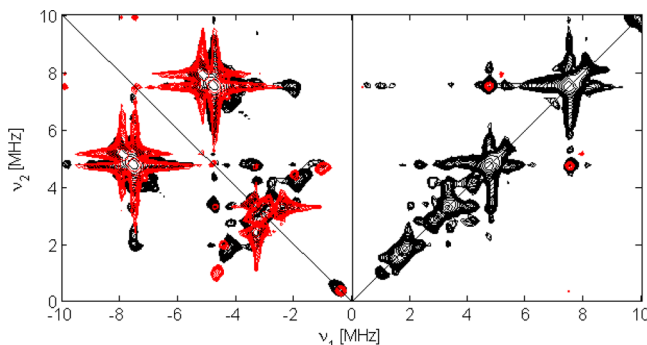


Figure 8. Experimental (black) and simulated (red) X-band ^{14}N HYSCORE spectrum of a frozen solution of the LS1 contribution of ferric MaCld at pH 9.75 recorded at an observer position corresponding with $g = g_z$. The spectra are the sum of the HYSCORE spectra for interpulse distance $\tau = 88, 96, 176$, and 200 ns. The simulation includes the contributions of the heme and His ^{14}N nuclei contributions (Table 5).

in LSAz1 an azide anion. Comparison of the current data with the limited data available for the azide complex of hhMb^{45,46} reveals mainly a difference in the values for the His nitrogens (Table 5). However, we should treat the latter data for hhMbN₃ with caution, since they are obtained from three-pulse ESEEM data only, which are known to be less resolved than HYSCORE data.⁴⁶

In an effort to determine the hyperfine and nuclear quadrupole parameters of the azide nitrogen nuclei in LSAz1, HYSCORE experiments were performed for MaCld complexed with $^{14}\text{N}_3^-$ and with terminally $1-^{15}\text{N}$ -labeled azide (Supporting Information). Although the spectral differences were very small, a set of cross peaks at (2.67, 4.37) MHz in the HYSCORE spectrum at $g = g_z$ could be unambiguously ascribed to the azide ^{14}N contribution (Figure S17). Assuming that these are double-quantum cross peaks, the hyperfine value for this orientation is ~1.8 MHz, with conditions for the nuclear quadrupole coupling: $2.63 \text{ MHz} \leq e^2 qQ/h \leq 3.04 \text{ MHz}$ for $1 \geq \eta \geq 0$.⁴⁷ The quadrupole interaction is considerably higher than observed for the heme, His₁₇₀ and Im ^{14}N ($e^2 qQ/h = 1.6-1.8 \text{ MHz}$, Tables 5 and 6). Earlier nuclear quadrupole measurements of HN₃ found a value of $e^2 qQ/h = 4.9 \text{ MHz}$ for the H-bound ^{14}N nucleus and $e^2 qQ/h = 1.4 \text{ MHz}$ for the other terminal nitrogen,⁴⁸ indicating that a large nuclear quadrupole value is realistic for the iron-bound ^{14}N of the azide ligand. To our knowledge, no data has been so far reported for the hyperfine/quadrupole interaction parameters of these nitrogens

in other azide–heme complexes. It is unclear at present why it is so challenging to determine these contributions in detail.

No relevant differences between the HYSCORE and ENDOR spectra of frozen solutions of azide-ligated MaCld taken at pH 7.5 and 5.5 were found, but this may be due to the very low abundance of the LSAz2.

CONCLUSIONS

The current X-ray crystallography and EPR study focused on the binding of imidazole, thiocyanate, and azide to chlorite dismutase from *Magnetspirillum* sp. MaCld is very open to distal ligand binding. The high resolution crystal structures of MaCld_N₃⁻ and MaCld_SCN⁻ show the ligands bound to the heme Fe atom through the N atom, with ~2 Å Fe–N bond distances. Not only does MaCld readily bind ligands, such as imidazole, azide, and thiocyanate, to form low-spin ferric heme complexes, but a variety of EPR signals due to such low-spin heme complexes are also observed in frozen solutions of wild-type MaCld at different pH values. Some of these complexes can be identified as hydroxide-ligated complexes. One low-spin heme form is found to inactivate the protein for further ligand binding. Its CW-EPR features are similar to those of the imidazole complex of MaCld, but such binding can be ruled out in the present system. Another low-spin ferric heme form in the native protein is particularly interesting. A pulsed EPR study reveals interactions with close-by protons that are not observed for the imidazole or azide complexes of MaCld.

A detailed HYSCORE and ENDOR analysis of the imidazole and azide complexes of MaCld allowed determination of the hyperfine and nuclear quadrupole interactions of the ^1H and ^{14}N nuclei in the heme pocket region. The data match well with the X-ray crystallographic data on related complexes of MaCld and other chlorite dismutases. Furthermore, all EPR data were in detail compared to reported data on different heme proteins, when available.

The data reported here allowed an exhaustive characterization of the Cld active site, unveiling the binding modes of different ligands to the enzyme's active site. The combination of X-ray crystallography and CW- and pulsed EPR revealed complementary information. This gives insight into the inner working of Cld at a molecular level, which is of importance for the development of potential biotechnological applications and synthetic mimics.

ASSOCIATED CONTENT

S Supporting Information

The Supporting Information is available free of charge on the ACS Publications website at DOI: 10.1021/acs.jpcb.5b04141.

Table 6. Principal ^{14}N Hyperfine (A) and Quadrupole (Q) Values of Azide-Ligated MaCld (LSAz1) (This Work) in Comparison with Those of hhMbN₃^{45,46 a}

	A_x (MHz)	A_y (MHz)	A_z (MHz)	Q_x (MHz)	Q_y (MHz)	Q_z (MHz)	α, β, γ (deg)
MaCld - LSAz1							
heme 1	-5.4 (± 0.2)	-5 (± 0.2)	-5.8 (± 0.1)	-0.52 (± 0.05)	0.85 (± 0.10)	-0.33 (± 0.05)	45, 0, 0 (± 10)
heme 2	-5.4 (± 0.2)	-5.0 (± 0.2)	-6.3 (± 0.1)	-0.52 (± 0.05)	0.85 (± 0.10)	-0.33 (± 0.05)	-45, 0, 0 (± 10)
His	-5.3 (± 0.2)	-5.7 (± 0.2)	-4.8 (± 0.1)	0.68 (± 0.05)	0.12 (± 0.05)	-0.80 (± 0.10)	90, 0, 0 (± 20)
hhMbN ₃							
heme 1 ⁴⁵	n.d.	n.d.	-5.64 (± 0.1)	n.d.	n.d.	-0.55 (± 0.1)	n.d.
heme 2 ⁴⁵	n.d.	n.d.	-6.14 (± 0.1)	n.d.	n.d.	-0.62 (± 0.1)	n.d.
His ⁴⁶	-4.6	-4.6	-3.0	0.44	0.36	-0.80	0, 10, 0

^aThe Euler angles α , β , and γ in the g -tensor frame are given. n.d. = not determined.

CW-EPR spectra of the ferric heme forms in wild-type *MaCld* at different pH values, EPR-spectral changes induced by azide binding, field-swept EPR analysis of LSIm, detailed view of the heme-pocket region of the imidazole complex of *NdCld*, full ¹⁴N HYSCORE analyses of LSIm and LSAz1, and comparison of ¹H ENDOR and HYSCORE spectra of LS1, LSIm, and LSAz1 (PDF)

AUTHOR INFORMATION

Corresponding Authors

*E-mail: pgonzalez@fbcn.unl.edu.ar. Phone/Fax: +54 342 4575213.

*E-mail: sabine.vandoorslaer@ua.ac.be. Phone: +32 3 2652461. Fax: +32 3 2652470.

Present Address

[†]European Molecular Biology Laboratory (EMBL), Notkestraße 85, 22603 Hamburg, Germany.

Author Contributions

^{||}These authors contributed equally.

Notes

The authors declare no competing financial interest.

ACKNOWLEDGMENTS

The research leading to these results has received funding from FCT through the project POCTI/QUI/55435/2004, grant no. Pest-C/EQB/LA0006/2011, grant no. UID/Multi/04378/2013, the European Community's Seventh Framework Programme (FP7/2007-2013) under BioStruct-X (grant agreement N°283570), and FWO/MINCyT (International exchange project VS.005.14N). A.D.S. thanks the Agency for Innovation by Science and Technology in Flanders (IWT) for PhD funding. H.D.C. thanks Fundação para a Ciência e a Tecnologia (FCT) for the fellowship SFRH/BD/86796/2012. D.M.F. and P.J.G. thank Fundação Calouste Gulbenkian for the award Programa de Estímulo à Investigação. M.G.R. and P.J.G. are members of CONICET (Argentina). We thank the beamline scientists of ID23-1 from the ESRF and of PXIII from SLS for their assistance in X-ray data collection.

REFERENCES

- (1) Hofbauer, S.; Schaffner, I.; Furtmüller, P. G.; Obinger, C. Chlorite Dismutases – a Heme Enzyme Family for Use in Bioremediation and Generation of Molecular Oxygen. *Biotechnol. J.* **2014**, *9*, 461–473.
- (2) Coates, J. D.; Achenbach, L. A. Microbial Perchlorate Reduction: Rocket-Fuelled Metabolism. *Nat. Rev. Microbiol.* **2004**, *2*, 569–580.
- (3) Maixner, F.; Wagner, M.; Lücker, S.; Pelletier, E.; Schmitz-Esser, S.; Hace, K.; Speck, E.; Konrat, R.; Le Paslier, D.; Daims, H. Environmental Genomics Reveals a Functional Chlorite Dismutase in the Nitrite-Oxidizing Bacterium ‘*Candidatus Nitrospira defluvii*’. *Environ. Microbiol.* **2008**, *10*, 3043–3056.
- (4) Mlynek, G.; Sjöblom, B.; Kostan, J.; Füreder, S.; Maixner, F.; Gysel, K.; Furtmüller, P. G.; Obinger, C.; Wagner, M.; Daims, H.; et al. Unexpected Diversity of Chlorite Dismutases: a Catalytically Efficient Dimeric Enzyme from *Nitrobacter winogradskyi*. *J. Bacteriol.* **2011**, *193*, 2408–2415.
- (5) Lee, A. Q.; Streit, B. R.; Zdilla, M. J.; Abu-Omar, M. M.; DuBois, J. L. Mechanism of an Exquisite Selectivity for O-O Bond Formation by the Heme-Dependent Chlorite Dismutase. *Proc. Natl. Acad. Sci. U. S. A.* **2008**, *105*, 15654–15659.
- (6) Bardya, N.; Bae, J.-H. Dissimilatory Perchlorate Reduction: A Review. *Microbiol. Res.* **2011**, *166*, 237–254.
- (7) Celis, A. I.; Geeraerts, Z.; Ngamenterebo, D.; Machovina, M. M.; Kurker, R. C.; Rajakumar, K.; Ivancich, A.; Rodgers, K. R.; Lukat-Rodgers, G. S.; DuBois, J. L. A Dimeric Chlorite Dismutase Exhibits O₂-Generating Activity and Acts as a Chlorite Antioxidant in *Klebsiella pneumoniae* MGH 78578. *Biochemistry* **2015**, *54*, 434–446.
- (8) Schaffner, I.; Hofbauer, S.; Krutzler, M.; Pirker, K. F.; Bellei, M.; Stadlmayr, G.; Mlynek, G.; Djinovic-Carugo, K.; Battistuzzi, G.; Furtmüller, P. G.; et al. Dimeric Chlorite Dismutase from the Nitrogen-Fixing Cyanobacterium *Cyanothece* sp. PCC7425. *Mol. Microbiol.* **2015**, *96*, 1053–1068.
- (9) Stenkel, K.; Thorell, H. D.; Bergius, H.; Aasa, R.; Nilsson, T. Chlorite Dismutase from *Ideonella dechloratans*. *JBIC, J. Biol. Inorg. Chem.* **2001**, *6*, 601–607.
- (10) Mehboob, F.; Wolterink, A. F.; Vermeulen, A. J.; Jiang, B.; Hagedoorn, P. L.; Stams, A. J.; Kengen, S. W. Purification and Characterization of a Chlorite Dismutase from *Pseudomonas chloritidismutans*. *FEMS Microbiol. Lett.* **2009**, *293*, 115–121.
- (11) Goblirsch, B. R.; Streit, B. R.; DuBois, J. L.; Wilmot, C. M. Structural Features Promoting Dioxygen Production by *Dechloromonas aromatic* Chlorite Dismutase. *JBIC, J. Biol. Inorg. Chem.* **2010**, *15*, 879–888.
- (12) Kostan, J.; Sjöblom, B.; Maixner, F.; Mlynek, G.; Furtmüller, P. G.; Obinger, C.; Wagner, M.; Daims, H.; Djinović-Carugo, K. Structural and Functional Characterization of the Chlorite Dismutase from the Nitrite-Oxidizing Bacterium “*Candidatus Nitrospira defluvii*”: Identification of a Catalytically Important Amino Acid Residue. *J. Struct. Biol.* **2010**, *172*, 331–342.
- (13) Freire, D. M.; Rivas, M. G.; Dias, A. M.; Lopes, A. T.; Costa, C.; Santos-Silva, T.; Van Doorslaer, S.; González, P. J. The Homopentameric Chlorite Dismutase from *Magnetospirillum* sp. *J. Inorg. Biochem.* **2015**, *151*, 1–9.
- (14) de Geus, D. C.; Thomassen, E. A.; Hagedoorn, P.-L.; Pannu, N. S.; van Duijn, E.; Abrahams, J. P. Crystal Structure of Chlorite Dismutase, a Detoxifying Enzyme Producing Molecular Oxygen. *J. Mol. Biol.* **2009**, *387*, 192–306.
- (15) Höfer, P.; Grupp, A.; Nebenführ, H.; Mehring, M. Hyperfine Sublevel Correlation (HYSCORE) Spectroscopy – A 2D Electron-Spin-Resonance Investigation of the Squaric Acid Radical. *Chem. Phys. Lett.* **1986**, *132*, 279–282.
- (16) Mims, W. B. Pulsed ENDOR Experiments. *Proc. R. Soc. London, Ser. A* **1965**, *283*, 452–457.
- (17) Davies, E. R. A New Pulse ENDOR Technique. *Phys. Lett. A* **1974**, *47*, 1–2.
- (18) Stoll, S.; Schweiger, A. EasySpin, a Comprehensive Software Package for Spectral Simulation and Analysis in EPR. *J. Magn. Reson.* **2006**, *178*, 42–55.
- (19) Kabsch, W. XDS. *Acta Crystallogr., Sect. D: Biol. Crystallogr.* **2010**, *66*, 125–132.
- (20) Evans, P. R.; Murshudov, G. N. How Good Are My Data and What Is the Resolution? *Acta Crystallogr., Sect. D: Biol. Crystallogr.* **2013**, *69*, 1204–1214.
- (21) Winn, M. D.; Ballard, C. C.; Cowtan, K. D.; Dodson, E. J.; Emsley, P.; Evans, P. R.; Keegan, R. M.; Krissinel, E. B.; Leslie, A. G. W.; McCoy, A.; et al. Overview of the CCP4 Suite and Current Developments. *Acta Crystallogr., Sect. D: Biol. Crystallogr.* **2011**, *67*, 235–242.
- (22) McCoy, A. K.; Grosse-Kunstleve, R. W.; Adams, P. D.; Winn, M. D.; Soroni, L. C.; Read, R. J. Phase Crystallographic Software. *J. Appl. Crystallogr.* **2007**, *40*, 658–674.
- (23) Murshudov, G. N.; Skubak, P.; Lebedev, A. A.; Pannu, N. S.; Steiner, R. A.; Nicholls, R. A.; Winn, M. D.; Long, F.; Vagin, A. A. REFMAC5 for the Refinement of Macromolecular Crystal Structures. *Acta Crystallogr., Sect. D: Biol. Crystallogr.* **2011**, *67*, 355–367.
- (24) Emsley, P.; Lohkamp, B.; Scott, W. G.; Cowtan, K. Features and Development of Coot. *Acta Crystallogr., Sect. D: Biol. Crystallogr.* **2010**, *66*, 486–501.
- (25) Joosten, R. P.; Joosten, K.; Murshudov, G. N.; Perrakis, A. PDB_RED: Constructive Validation, More than Just Looking for Errors. *Acta Crystallogr., Sect. D: Biol. Crystallogr.* **2012**, *68*, 484–496.

- (26) Laskowski, R. A.; MacArthur, M. W.; Moss, D. S.; Thornton, J. M. Procheck – A Program to Check the Stereochemical Quality of Protein Structures. *J. Appl. Crystallogr.* **1993**, *26*, 283–291.
- (27) Chen, V. B.; Arendall, W. B., 3rd; Headd, J. J.; Keedy, D. A.; Immormino, R. M.; Kapral, G. J.; Murray, L. W.; Richardson, J. S.; Richardson, D. C. MolProbity – All-Atom Structure Validation for Macromolecular Crystallography. *Acta Crystallogr., Sect. D: Biol. Crystallogr.* **2010**, *66*, 12–21.
- (28) Goodin, D. B.; McRee, D. E. The Asp-His-Fe Triad of Cytochrome c Peroxidase Controls the Reduction Potential, Electronic Structure, and Coupling of the Tryptophan Free Radical to the Heme. *Biochemistry* **1993**, *32*, 3313–3324.
- (29) Hofbauer, S.; Bellei, M.; Sündermann, A.; Pirker, K. F.; Hagnmüller, A.; Mlynek, G.; Kostan, J.; Daims, H.; Furtmüller, P. G.; Djinović-Carugo, K.; et al. C. Redox Thermodynamics of High-Spin and Low-Spin Forms of Chlorite Dismutases with Diverse Subunit and Oligomeric Structures. *Biochemistry* **2012**, *51*, 9501–9512.
- (30) Danielsson Thorell, H.; Beyer, N. H.; Heegaard, N. H. H.; Öhman, M.; Nilsson, T. Comparison of Native and Recombinant Chlorite Dismutase from *Ideonella dechloratans*. *Eur. J. Biochem.* **2004**, *271*, 3539–3546.
- (31) Svistunenko, D. A.; Worall, J. A. R.; Chugh, S. B.; Haigh, S. C.; Ghiladi, R. A.; Nicholls, P. Ferric Haem Forms of *Mycobacterium tuberculosis* Catalase-Peroxidase Probed by EPR Spectroscopy: Their Stability and Interplay with pH. *Biochimie* **2012**, *94*, 1274–1280.
- (32) Hagedoorn, P. L.; de Geus, D. C.; Hagen, W. R. Spectroscopic Characterization and Ligand-Binding Properties of Chlorite Dismutase from the Chlorate Respiring Bacterial Strain GR-1. *Eur. J. Biochem.* **2002**, *269*, 4905–4911.
- (33) Blanc, B.; Mayfield, J. A.; McDonald, C. A.; Lukat-Rodgers, G. S.; Rodgers, K. R.; DuBois, J. L. Understanding How the Distal Environment Directs Reactivity in Chlorite Dismutase: Spectroscopy and Reactivity of Arg183 Mutants. *Biochemistry* **2012**, *51*, 1895–1910.
- (34) Torii, K.; Iizuka, T.; Ogura, Y. Magnetic Susceptibility and EPR Measurements of Catalase and its Derivates. A Thermal Equilibrium between the High- and Low-Spin States in the Catalase-Azide Compound. *J. Biochem.* **1970**, *68*, 837–841.
- (35) Hori, H. Analysis of the Principal g-Tensors in Single Crystals of Ferrimyoglobin Complexes. *Biochim. Biophys. Acta, Protein Struct.* **1971**, *251*, 227–235.
- (36) Maurus, R.; Boguil, R.; Nguyen, N. T.; Mauk, A. G.; Brayer, G. Structural and Spectroscopic Studies of Azide Complexes of Horse Heart Myoglobin and the His-64 → Thr Variant. *Biochem. J.* **1998**, *332*, 67–74.
- (37) Sündermann, A.; Reif, M. M.; Hofbauer, S.; Obinger, C.; Oostenbrink, C. Investigation of Ion Binding in Chlorite Dismutases by Means of Molecular Dynamics Simulations. *Biochemistry* **2014**, *53*, 4869–4879.
- (38) Dickinson, L. C.; Chien, J. C. Electron Paramagnetic Resonance Study of Carp Methemoglobin. *J. Biol. Chem.* **1977**, *252*, 1327–1330.
- (39) Van Doorslaer, S.; van den Bosch, M.; Tillemans, L.; Dewilde, S. EPR Analysis of Imidazole Binding to *Methanosarcina acetivorans* Protoglobin. *Appl. Magn. Reson.* **2015**, *46*, 421–433.
- (40) Walker, F. A. Magnetic Spectroscopic (EPR, ESEEM, Mössbauer, MCD and NMR) Studies of Low-Spin Ferriheme Centers and Their Corresponding Heme Proteins. *Coord. Chem. Rev.* **1999**, *185–186*, 471–534.
- (41) García-Rubio, I.; Mitrikas, G. Structure and Spin Density of Ferric Low-Spin Heme Complexes Determined with High-Resolution ESEEM Experiments at 35 GHz. *JBIC, J. Biol. Inorg. Chem.* **2010**, *15*, 929–941.
- (42) Vinck, E.; Van Doorslaer, S. Analysing Low-Spin Ferric Complexes Using Pulse EPR Techniques: a Structure Determination of Bis(4-methylimidazole)-tetraphenylporphyrinatoiron(iii). *Phys. Chem. Chem. Phys.* **2004**, *6*, 5324–5330.
- (43) Scholes, C. P.; Falkowski, K. M.; Chen, S. Bank, J. Electron Nuclear Double Resonance (ENDOR) of Bis(imidazole) Ligated Low-Spin Ferric Heme Systems. *J. Am. Chem. Soc.* **1986**, *108*, 1660–1671.
- (44) Pöppl, A.; Kevan, L. A Practical Strategy for Determination of Proton Hyperfine Interaction Parameters in Paramagnetic Transition Metal Ion Complexes by Two-Dimensional HYSCORE Electron Spin Resonance Spectroscopy in Disordered Systems. *J. Phys. Chem.* **1996**, *100*, 3387–3394.
- (45) Mulks, C. F.; Scholes, C. P.; Dickinson, L. C.; Lapidot, A. Electron Nuclear Double Resonance from High- and Low-Spin Ferric Hemoglobins and Myoglobins. *J. Am. Chem. Soc.* **1979**, *101*, 1645–1654.
- (46) Magliozzo, R. S.; Peisach, J. Evaluation of Nitrogen Nuclear Hyperfine and Quadrupole Coupling Parameters for the Proximal Imidazole in Myoglobin-Azide, -Cyanide, and -Mercaptoethanol Complexes by Electron Spin Echo Envelope Modulation Spectroscopy. *Biochemistry* **1993**, *32*, 8446–8456.
- (47) Dikanov, S. A.; Xun, L.; Karpiel, A. B.; Tyryshkin, A. M.; Bowman, M. K. Orientationally-Selected Two-Dimensional ESEEM Spectroscopy of the Rieske-Type Iron-Sulfur Cluster in 2,4,5-Trichlorophenoxyacetate Monooxygenase from *Burkhoderia cepacia* AC1100. *J. Am. Chem. Soc.* **1996**, *118*, 8408–8416.
- (48) Murgich, J.; Aray, Y. ¹⁴N Nuclear Quadrupole Resonance and Ab Initio MO Study of Organic Azides. *J. Chem. Phys.* **1987**, *87*, 115–117.